ELSEVIER

Applied Acoustics 62 (2001) 841–865

applied acoustics

www.elsevier.com/locate/apacoust

Estimation of object location and radius of curvature using ultrasonic sonar

Ali Şafak Sekmen [a,*], Billur Barshan [b]

[a] *Department of Electrical and Computer Engineering, Vanderbilt University, Station B, Box 1836, Nashville TN 37235, USA*

[b] *Department of Electrical Engineering, Bilkent University, Bilkent, 06533 Ankara, Turkey*

Received 1 August 1999; received in revised form 17 July 2000; accepted 19 July 2000

Abstract

Acoustic sensors are very popular in time-of-flight (TOF) ranging systems since they are inexpensive and convenient to use. One of the major limitations of these sensors is their low angular resolution which makes object localization difficult. In this paper, an adaptive multi-sensor configuration consisting of three transmitter/receiver ultrasonic transducers is introduced to compensate for the low angular resolution of sonar sensors and improve the localization accuracy. With this configuration, the radius of curvature and location of cylindrical objects are estimated. Two methods of TOF estimation are considered: thresholding and curve-fitting. The bias-variance combinations of these estimators are compared. Theory and simulations are verified by experimental data from a real sonar system. Extended Kalman filtering is used to smooth the data. It is shown that curve-fitting method, compared to thresholding method, provides about 30% improvement in the absence of noise and 50% improvement in the presence of noise. Moreover, the adaptive configuration improves the estimation accuracy by 35–40%.

Keywords: Ultrasonic transducer; Time-of-flight; Extended Kalman filter; Target discrimination

1. Introduction

Ultrasonic transducers have been widely used in TOF ranging systems. However, these sensors are limited by their large beamwidth which makes accurate localization of objects difficult. Multiple reflections may also be difficult to interpret. Many researchers have developed different approaches for improved ultrasonic sensing.

* Corresponding author. Tel.: +1-615-963-5712; fax: +1-615-963-2165.
E-mail address: sekmen@vuse.vanderbilt.edu (A.S. Şafak).

0003-682X/01/$ - see front matter
PII: S0003-682X(00)00077-3

For target discrimination and accurate object recognition, Barshan and Kuc differentiated sonar reflections from corners and planes by using a multi-transducer sensing system [1]. In [2], Kleeman and Kuc classified the target primitives as plane, corner, edge and unknown, and showed that in order to distinguish these, two receivers and two transmitters are necessary and sufficient in a non-adaptive configuration. In[3], Kleeman and Akbarally used a sonar sensor for classifying and discriminating target primitives commonly occurring in 3-D space. Kuc fused sonar information using a system that adaptively changes its position and configuration in response to the echoes it detects [4–6].

Sonar data have also been combined with other types of sensory information to improve robot localization and map building systems. Flynn combined infrared and sonar sensors to compensate for the low angular resolution of sonar sensors [7]. Curran and Kyriakopoulos also combined sonar and infrared sensor data with dead-reckoning by using an extended Kalman filter to estimate current location of a mobile robot [8]. Peremans et al. [9] and Sabatini [10] investigated curved reflectors using a linear sonar array configuration. Ohya and Yuta showed how the information obtained by an ultrasonic transducer is affected by the characteristics of the sensing systems such as its sensitivity and directivity [11]. In [12], Sabatini illustrated that advanced filtering methods are required for making data more accurate and reliable. He also proposed a digital-signal-processing technique for building a transducer array capable of automatically compensating for variations in the speed of sound due to temperature or any other atmospheric conditions [13]. Webb et al. used ultrasonic arrays to measure the range and bearing of a target and guide a mobile robot [14]. Ko et al. developed a system using acoustic transducers to extract multiple landmarks for the indoor navigation of a mobile robot [15]. In addition, other researchers have used adaptive sonar arrays to add flexibility to their systems [16]. An alternative to using multiple transducers is to use a single transducer and keep changing its position as in synthetic aperture radar systems [17].

In this paper, an adaptive system consisting of three transducers is used to improve the location and radius of curvature estimation accuracy in 2-D. The main contributions of this paper are the presentation of a new technique for the estimation of radius of curvature and the further improvement of this estimate through the use of an adaptive configuration. For TOF estimation, simple thresholding and curve-fitting methods are employed. In [18], simple thresholding, double thresholding, curve-fitting, sliding window, and matched filter TOF estimation techniques are compared and it is concluded that although the matched filter method is optimal, simpler, faster yet suboptimal techniques provide a variety of attractive compromises between measurement accuracy and system complexity.

When the reflection point of the object is not along the line-of-sight (LOS) of the ultrasonic transducer, there is a decline (as $e^{-k\theta 2}$, where θ is the deviation angle and k is a constant depending on the beamwidth of the transducer) in the amplitude of the reflected sonar signal, which decreases the signal-to-noise ratio (SNR) [see Eq. (4)]. In order to avoid this problem and increase the localization accuracy, an adaptive multi-sensor configuration composed of three transmitting/receiving transducers is used as shown in Fig. 2. Depending on the location of the object, the

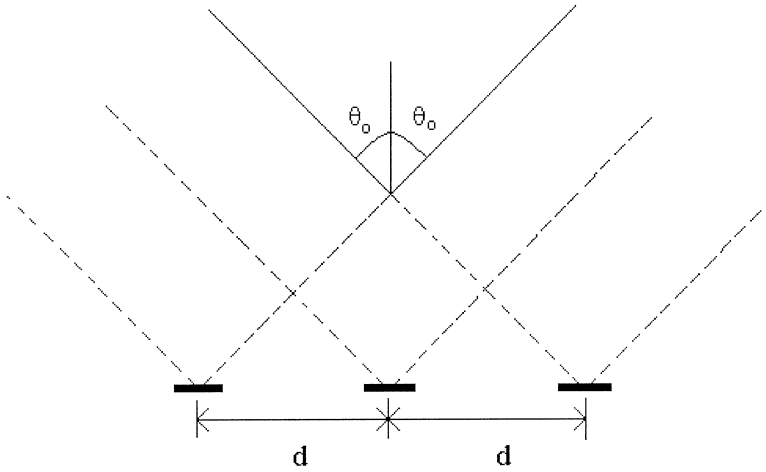

Fig. 1. The beam patterns of the transducers (within dashed lines) and the sensitivity region (within solid lines).

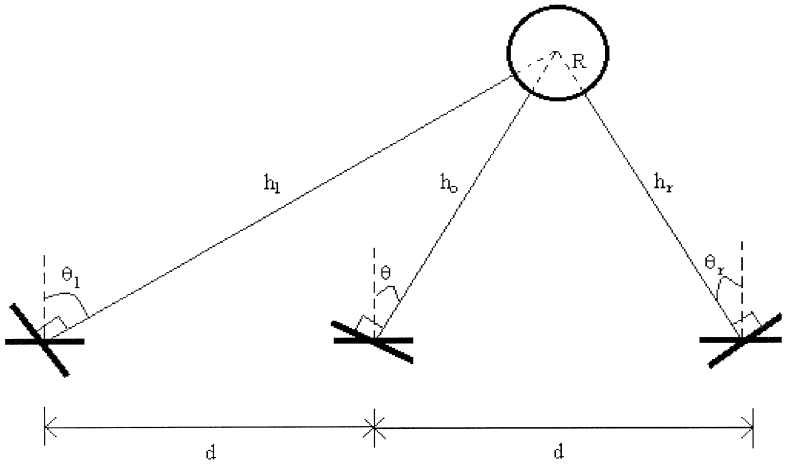

Fig. 2. The object and sensor configuration.

sensor can rotate its transducers around their centers towards the target to obtain a higher SNR. This way, the radius of curvature and location estimates of the reflecting objects — compared to the nonadaptive system — are improved. With the estimation of radius of curvature, different types of reflectors such as walls, cylinders and edges can be discriminated. For large values of radius, the object is classified as a planar wall, and for values close to zero, the object is classified as an edge. The extended treatment of 3-D target differentiation can be found in [19].

In Section 2, basic concepts of sonar sensing are reviewed and the main reason for using an adaptive configuration is discussed. In Section 3.1, the algorithm for the radius of curvature and location estimation is given. In order to estimate TOF, two

simple, fast, but suboptimal methods are used: conventional *thresholding* method and *curve-fitting* method. These methods are described in Section 3.2. Also, a 100-realization Monte Carlo simulation study is performed to obtain more reliable results in noisy environments. The simulation results are presented in Section 3.3. In Section 3.4, in order to evaluate the performance of the estimators, a comparison of their bias-variance combinations is presented. Extended Kalman filter method, used for smoothing the sonar data, is explained in Section 4 and the experimental results are presented in Section 5. Finally, conclusions are drawn and directions for future work are motivated in Section 6.

2. Sonar sensing

2.1. Acoustic reflection

In most commonly employed sonar ranging systems, an echo is produced when a transmitted pulse encounters an object and a range value $h = \frac{ct_0}{2}$ is produced when the echo is detected by the receiver. Here, t_0 is the time-of-flight (TOF) of the echo signal and c is the speed of sound in air.[1]

The characteristics of the radiation pattern of an acoustic transducer are different in the neighborhood of the transducer (the near-field region or the Fresnel diffraction zone) and beyond the near-field (the far-field region or the Fraunhofer zone [20]). The expression for the sound pressure within the near-field is relatively complex, and not within the scope of this paper. The far-field characteristics at range h and angular deviation θ from the line-of-sight for a *single* frequency of excitation is described by [21,22]

$$A(h,\theta) = \frac{p_{\max} h_{\min}}{h} \frac{J_1(ka\sin\theta)}{ka\sin\theta} \quad \text{for } h \geqslant h_{\min} \tag{1}$$

where $J_1()$ is the Bessel function of first order, and $P_{\max}$ is the propagation pressure amplitude on the beam axis at range $h_{\min}$ along the line-of-sight.

The half beamwidth θ_0 in the far-field region corresponds to the first zero of the Bessel function in Eq. (1) which occurs at $ka\sin\theta = 1.22\pi$ and the following equation is obtained for the half beamwidth angle [23]:

$$\theta_0 = \sin^{-1}\left[\frac{0.61\lambda}{a}\right] \tag{2}$$

where $\lambda = c/f_0$ is the wavelength (f_0 is the resonance frequency) and a is the transducer aperture radius.

[1] $c = 331.4\sqrt{\frac{T}{273}}$ m/s, where T is the absolute temperature in Kelvin. At room temperature, $c = 343.3$ m/s.

Since a range of frequencies around f_0 are transmitted, the corresponding beam patterns are superposed and the resulting beam pattern can be approximated by a Gaussian beam profile centered around zero with standard deviation $\sigma_\theta = \frac{\theta_0}{2}$ [22, 24]:

$$\bar{A}_{h,\theta} = \frac{P_{\max} h_{\min}}{h} e^{\frac{\theta^2}{2\sigma_\theta^2}} \text{ for } h \geqslant h_{\min} \tag{3}$$

For a cylindrical target at range h and making an angle θ with the LOS of an ultrasonic transducer, the received time signal reflected by the target is a sinusoidal enveloped by a Gaussian which is given by [22,25,26]:

$$s_{h,\theta}(t) = \rho_c \frac{A_{\max} h_{\min}^{3/2}}{h^{3/2}} e^{-\frac{\theta^2}{\sigma_\theta^2 e} - \frac{\left(t - t_0 - \frac{3}{f_0}\right)^2}{2\sigma_t^2}} \sin[2\pi f_0 (t - t_0)] \quad h \geqslant h_{\min} \tag{4}$$

where h is the distance between the transducer and the surface of the object, ρ_c is the reflection coefficient that increases with radius of curvature, $A_{\max}$ is the maximum amplitude, $h_{\min} \cong a^2/\lambda$ (a is the radius of the transducer aperture), θ is the deviation angle from the LOS, $\sigma_\theta = \theta_0/2$ (is the half beamwidth angle), t_0 is the time-of-flight, f_0 is the resonance frequency, $\lambda = c/f_0$, and $\sigma_t = 1/f_0$.

2.2. Adaptive sensor configuration

In this study, a sensor configuration composed of three transducers is employed. Each one of the transducers is sensitive to echo signals reflected within its beam pattern. All members of the configuration can detect targets located within the overlap of the three beam patterns, which is called the sensitivity region, as illustrated in Fig. 1. The minimum distance at which a target is detectable by all three transducers is approximately $\frac{d-a}{\tan\theta_0} + \frac{a^2}{\lambda}$. This corresponds to the distance between the central transducer and the start of the joint sensitivity pattern.

Eq. (4) shows that when the object and the transducer LOS are not perpendicular to each other ($\theta \neq 0^\circ$), there is a decline in the amplitude which decreases the SNR. Hence, information provided by ultrasonic transducers is most reliable when the object lies along the LOS of the transducer, and at nearby ranges due to the $1/h^{3/2}$ term in Eq. (4). Because of this, the transducers are rotated adaptively around their centers to align the LOS with the target direction (Fig. 2).

3. Location and radius of curvature estimation

A cylindrical object with radius R and orientation θ is considered as shown in Fig. 2. In this figure, h_0 is the distance between the central transducer and the surface of the object. Likewise, h_1 and h_r are the distances between the surface of the object and the left and right transducers, respectively. θ, θ_l and θ_r are the deviation angles of the

central, left, and right transducers, respectively and d is the transducer separation. In this section, the following unknowns are estimated:

- The distance between the center of the object and the central transducer: $r = h_0 + R$.
- The deviation angle of the central transducer: θ.
- The radius of curvature: R.

3.1. Algorithm

The following relations hold true between the distances to the surface of the object and the quantities of interest listed above:

$$\begin{aligned} h_0 &= \frac{ct_0}{2} = r - R \\ h_r &= \frac{ct_r}{2} = \sqrt{r^2 + d^2 - 2dr\sin\theta} - R \\ h_l &= \frac{ct_l}{2} = \sqrt{r^2 + d^2 + 2dr\sin\theta} - R \end{aligned} \tag{5}$$

where h_0, h_r, h_l are the true distances to the surface of the object and t_0, t_r, t_l are the true TOF values. The following measurements are taken by the three transducers:

$$\begin{aligned} \bar{h}_0 &= h_0 + w_0 \\ \bar{h}_r &= h_r + w_r \\ \bar{h}_l &= h_l + w_l \end{aligned} \tag{6}$$

Here, $\bar{h}_0, \bar{h}_r, \bar{h}_l$ are the measured distances and w_0, w_r and w_l are spatially uncorrelated zero-mean white Gaussian noise for the central, right and left transducers, respectively. In [9], it is shown that for acoustic transducers, the noise correlation coefficient is small since most of the noise on the transducers is dominated by the thermal noise in the electronics. Because of this, w_0, w_r and w_l can be modeled as spatially uncorrelated Gaussian noise. Hence, the error correlation matrix, its inverse, and the probability density function of the measurement vector $\tilde{\boldsymbol{h}}$ are given as follows:

$$C = \begin{bmatrix} \sigma_{w_0}^2 & 0 & 0 \\ 0 & \sigma_{w_r}^2 & 0 \\ 0 & 0 & \sigma_{w_l}^2 \end{bmatrix} \tag{7}$$

$$C^{-1} = \begin{bmatrix} \dfrac{1}{\sigma_{w_0}^2} & 0 & 0 \\ 0 & \dfrac{1}{\sigma_{w_r}^2} & 0 \\ 0 & 0 & \dfrac{1}{\sigma_{w_l}^2} \end{bmatrix} \tag{8}$$

$$p\left(\tilde{\mathbf{h}}|r,\theta,R\right)=\frac{1}{2\pi|C|}\exp\left\{-\frac{1}{2}\left[\tilde{\mathbf{h}}-\mathbf{h}(r,\theta,R)\right]^{T}C^{-1}\left[\tilde{\mathbf{h}}-\mathbf{h}(r,\theta,R)\right]\right\} \tag{9}$$

where the vectors $\tilde{\mathbf{h}}$, $\mathbf{h}(r,\theta,R)$ and $\mathbf{n}$ are defined as follows:

$$\tilde{\mathbf{h}}\triangleq\begin{bmatrix}\tilde{h}_0\\ \tilde{h}_{\mathrm{r}}\\ \tilde{h}_{\mathrm{l}}\end{bmatrix}\quad \mathbf{h}(r,\theta,R)\triangleq\begin{bmatrix}r-R\\ \sqrt{r^2+d^2-2\mathrm{d}r\sin\theta}-R\\ \sqrt{r^2+d^2+2\mathrm{d}r\sin\theta}-R\end{bmatrix} w\triangleq\begin{bmatrix}w_0\\ w_{\mathrm{r}}\\ w_{\mathrm{l}}\end{bmatrix} \tag{10}$$

and are related by $\tilde{\mathbf{h}}=\mathbf{h}(\mathbf{r},\theta,\mathbf{R})+\mathrm{w}$. The r,θ and R values maximizing Eq. (9) are the maximum likelihood estimates which can be found by solving the equation set $\tilde{\mathbf{h}}=\mathbf{h}\left(\hat{r},\hat{\theta},\hat{R}\right)$ for $\hat{r},\hat{\theta}$, and $\hat{R}$:

$$\hat{r}=\frac{2d^2+2\left(\tilde{h}_{\mathrm{l}}+\tilde{h}_{\mathrm{r}}\right)\tilde{h}_0-2\tilde{h}_0^2-\tilde{h}_{\mathrm{l}}^2-\tilde{h}_{\mathrm{r}}^2}{2\tilde{h}_r+2h_l-4\tilde{h}_0} \tag{11}$$

$$\hat{\theta}=\sin^{-1}\left[\frac{\tilde{h}_{\mathrm{l}}^2-\tilde{h}_{\mathrm{r}}^2+2\left(\tilde{h}_{\mathrm{l}}-\tilde{h}_{\mathrm{r}}\right)\hat{R}}{4d\left[\tilde{h}_0+\hat{R}\right]}\right] \tag{12}$$

$$\hat{R}=\frac{\left(\tilde{h}_0^2+\tilde{h}_{\mathrm{l}}^2\right)-2\left(\tilde{h}_0^2+d^2\right)}{4\tilde{h}_0-2\left(\tilde{h}_{\mathrm{r}}+\tilde{h}_{\mathrm{l}}\right)} \tag{13}$$

The deviation angles of the left and right transducers are estimated by the following equations:

$$\hat{\theta}_{\mathrm{l}}=\sin^{-1}\left(\frac{\hat{r}_{\mathrm{l}}^2-\hat{r}^2+d^2}{2\mathrm{d}\hat{r}_{\mathrm{l}}}\right) \tag{14}$$

$$\hat{\theta}_{\mathrm{r}}=\sin^{-1}\left(\frac{\hat{r}_{\mathrm{r}}^2-\hat{r}^2+d^2}{2\mathrm{d}\hat{r}_{\mathrm{r}}}\right) \tag{15}$$

where $\hat{r}_{\mathrm{l}}=\tilde{h}_{\mathrm{l}}+\hat{R}$ and $\hat{r}_{\mathrm{r}}=\tilde{h}_{\mathrm{r}}+\hat{R}$. Finally, the left, central, and right transducers are rotated by $\hat{\theta}_{\mathrm{l}},\hat{\theta}$ and $\hat{\theta}_{\mathrm{r}}$, respectively, and r,θ, and R are estimated again.

In this paper, the adaptation process is completed in two steps: after the initial estimate is obtained with the flat configuration of the sensor, the transducers are rotated, and an improved estimate is made. The number of steps can be easily increased to further improve the accuracy of the final estimate. It is also possible to make the adaptation process continuous. This would particularly be suitable when the target position is not stationary and the target is in motion. In this case, we

envision that at every update, the transducers adapt their orientation according to the current target position and its estimated radius of curvature.

3.2. TOF estimation

In this study, two different TOF estimation methods are used: the *thresholding* and *curve-fitting* methods.

In thresholding TOF systems, an appropriate threshold τ is chosen and the first time instance at which the reflected signal exceeds this threshold is considered as the TOF. In order to reduce the error in the TOF estimations obtained from the thresholding method and improve the estimates, a curve-fitting approach is used. In this method, a parabolic curve of the form $a_o(t - t_0)^2$ is fitted to the onset of the sonar echo. First, initial estimates of the two parameters a_0 and t_0 are obtained by using samples of the signal around the thresholding point. Initial estimate for t_0 is found by simple thresholding, arid a_0 is estimated from the second derivative approximation around the threshold point [27]. The iterative Levenberg-Marquardt nonlinear least-squares algorithm is initialized by these values. In the simulations and the experiments, 50 samples of the echo signal, centered around the threshold point have been used to estimate the parameters a_0 and t_0 of the best-fitting curve. The value of t_0 finally obtained, which corresponds to the vertex of the parabola, is taken as an estimate of the TOF (Fig. 3). The curve-fitting estimate is expected to be more accurate than simple thresholding since it should reduce/eliminate the bias inherent to thresholding and also because it uses a larger portion of the signal (i.e. its onset rather than a single point at which threshold is exceeded).

3.3. Simulation results

In the simulations, Eq. (4) is used to model the signals and $A_{\max} = 1$, $h_{\min} = 5.8$ cm, $\rho_c = 0.45\,R - 0.022,$, $f_0 = 49.4$ kHz, and $c = 343.5$ m/s are used as the model parameters. Once the range r, the deviation angle θ, and the radius of curvature R are estimated from Eqs. (11)–(13), the transducers are rotated by the angles calculated using Eqs. (12), (14), and (15), respectively. Then the second estimates are calculated. In the simulations, 100-realization Monte-Carlo simulation study is employed. The mean values and the standard deviations from the mean values of r, θ, and R for the linear and rotated configurations are illustrated. In all the simulation results, dash-dot or dot lines correspond to the first (linear configuration) estimates, whereas solid lines correspond to the second (rotated configuration) estimates. Moreover, the mean of the estimates and mean±standard deviation (a) are shown in the simulation results.

Fig. 4 illustrates the radius of curvature estimates corresponding to the linear and rotated configurations versus the transducer separation d. Fig. 4(a) shows the estimates using the thresholding method in the absence of noise. As d increases, the error in both estimates decreases. The percentage error for the rotated position is 9.2%. Fig. 4(c) displays the same results in the presence of noise. Second estimate is approximately 40% better than the first estimate. The first estimate gets worse after

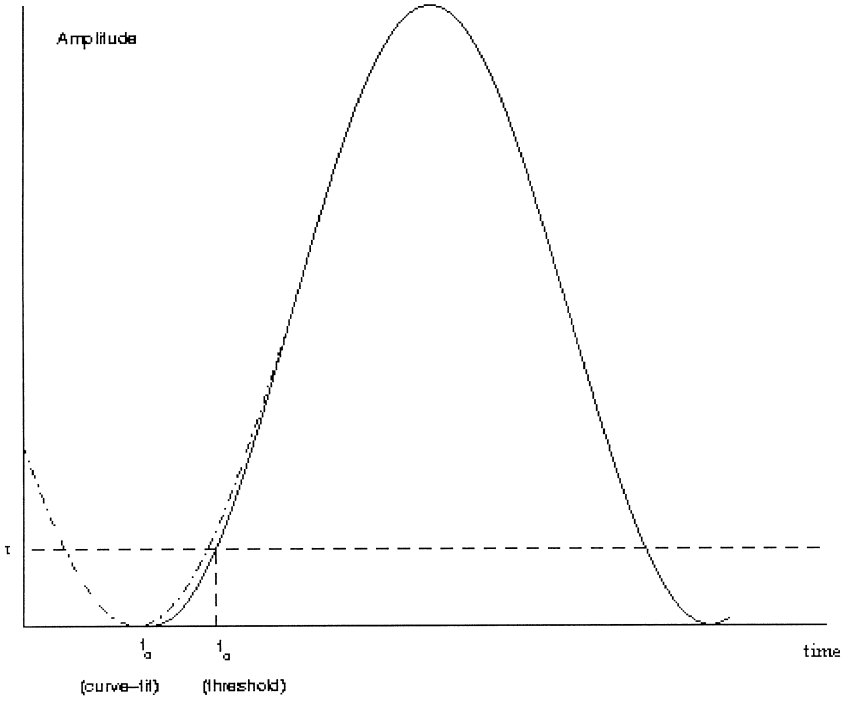

Fig. 3. Thresholding and curve-fitting methods to estimate the TOF.

$d = 8$ cm since the target is now located either at very low signal-to-noise ratio (SNR) regions of the sensitivity pattern or outside it. Fig. 4(b) illustrates the estimates using curve-fitting method in the absence of noise. Both estimates improve as d increases. The error for the rotated position is 0.4%. Fig. 4(d) shows the results using curve-fitting in the presence of noise. The second estimate is better than the first estimate. When Fig. 4(c) and (d) are compared it is observed that the curve-fitting method provides better estimates in the presence of noise. The improvement for the first estimate is approximately 60% and it is approximately 20% for the second estimate.

Fig. 5(a) and (b) illustrates how the range r depends on d and θ, respectively. Figs. 6(a) and (b) display θ estimates versus h_0 and R, respectively. The curve-fitting method is used to measure the TOF. $R = 5$ cm, $h_0 = 100$ cm, $d = 10$ cm, and $\theta = 5^\circ$ are considered and one variable is changed in each figure. Fig. 5(a) shows that the first estimation improves up to $d = 12$ cm and after that it worsens for the same reason given in the previous paragraph. In Fig. 5(b), when $\theta = 6^\circ$, the left transducer starts measuring incorrectly and when $\theta = 11^\circ$, the central transducer starts measuring incorrectly as well. As h_0 increases, the deviation angles of the left and right transducers decrease and estimates improve [Fig. 6(a)]. Fig. 6(b) displays that as the true radius R increases, the estimates and their standard deviations improve.

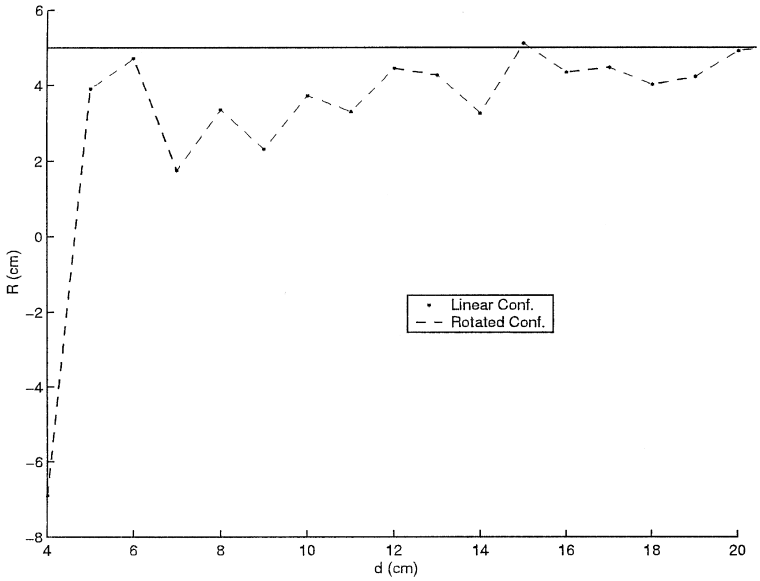

(a)

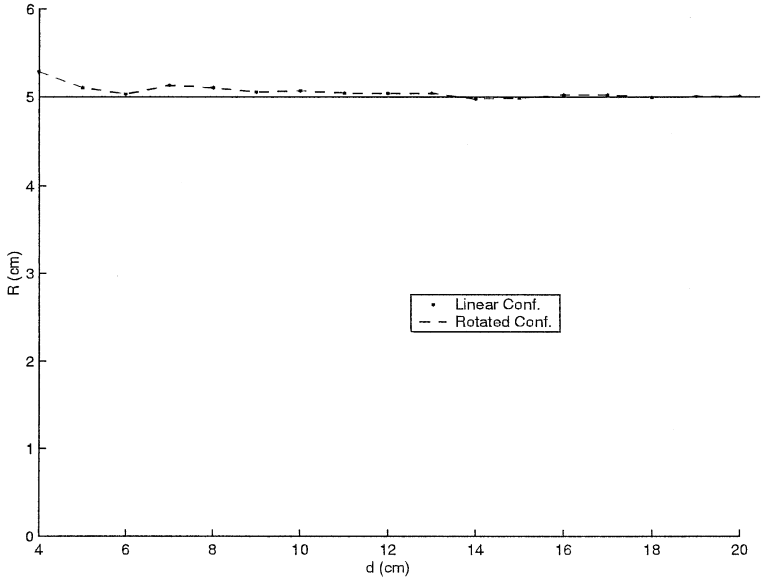

(b)

Fig. 4. Estimated radius versus d with thresholding (a,c) and curve-fitting (b,d) in the absence of noise (a,b) and in the presence of noise (c,d). Dash-dot and solid lines indicate the mean of the estimate and $\pm\sigma_r$ obtained at the flat and adapted positions, respectively (*Continued on next page*).

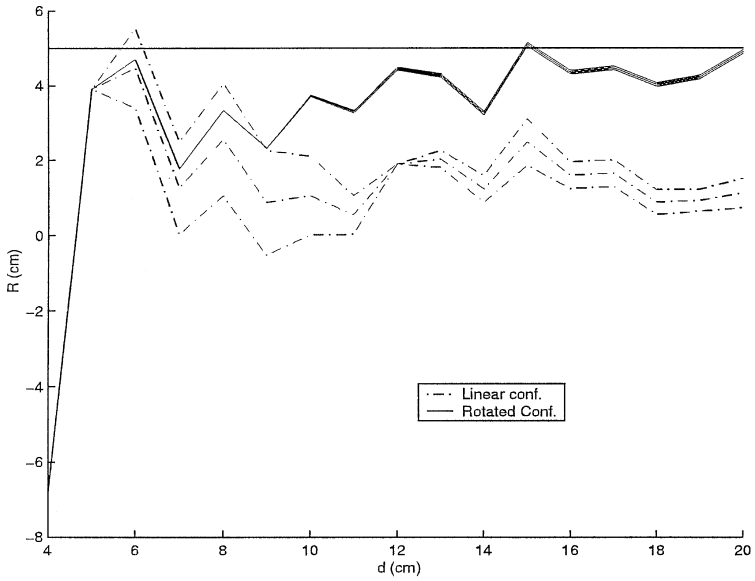

(c)

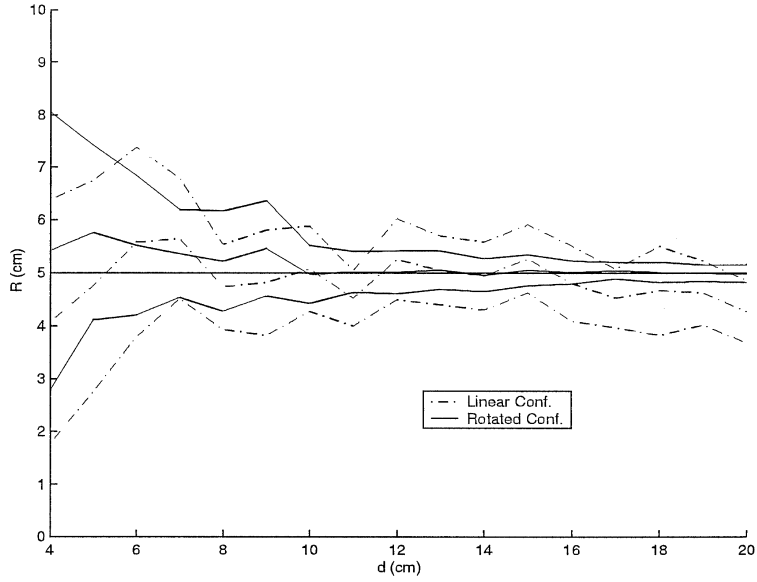

(d)

Fig. 4. (*continued*)

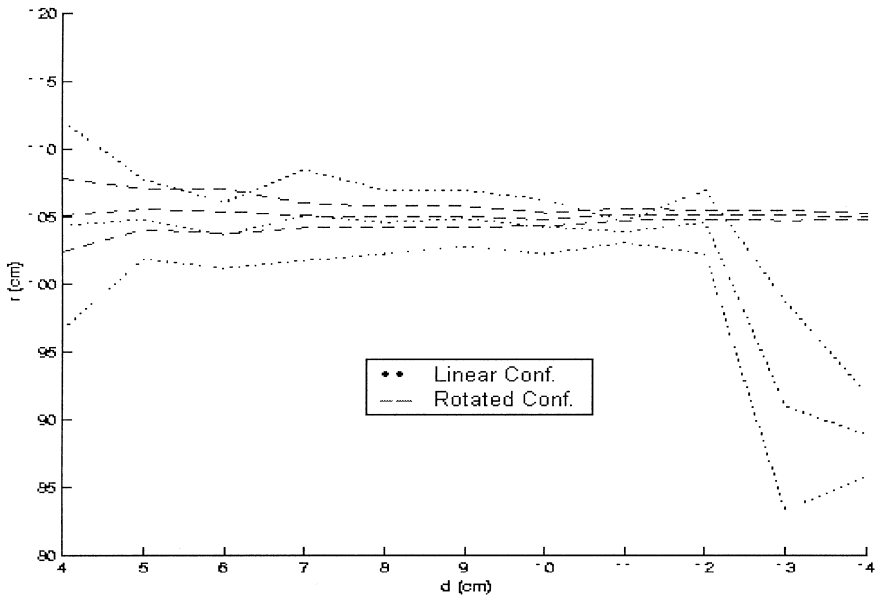

(a)

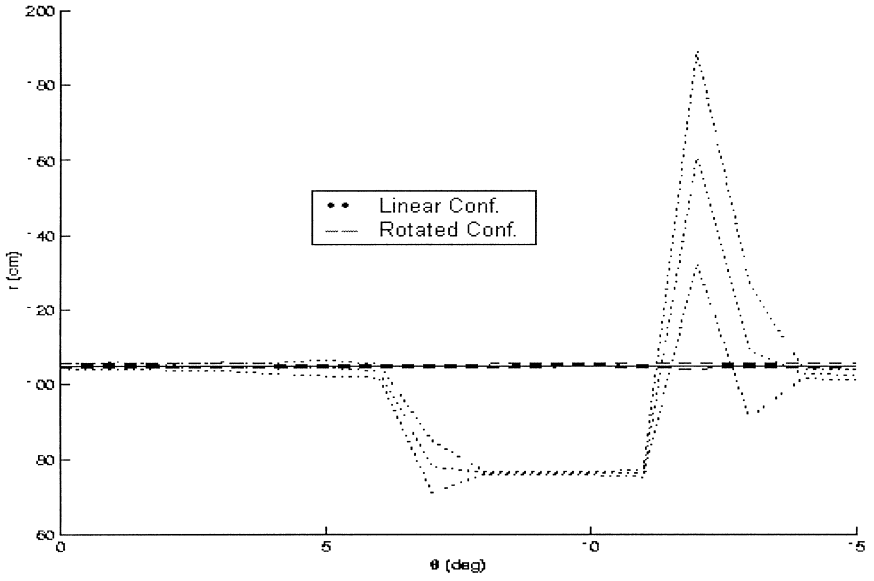

(b)

Fig. 5. Estimated range (r) versus (a) d, (b) θ, with curve-fitting. Dotted and dashed lines indicate the mean of the estimate and $\pm\sigma_r$ obtained at the flat and adapted positions, respectively.

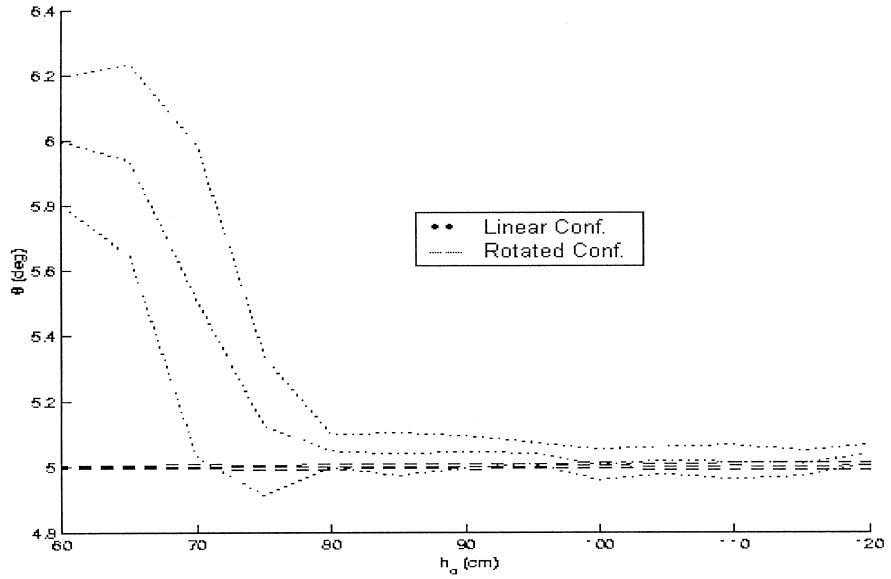

(a)

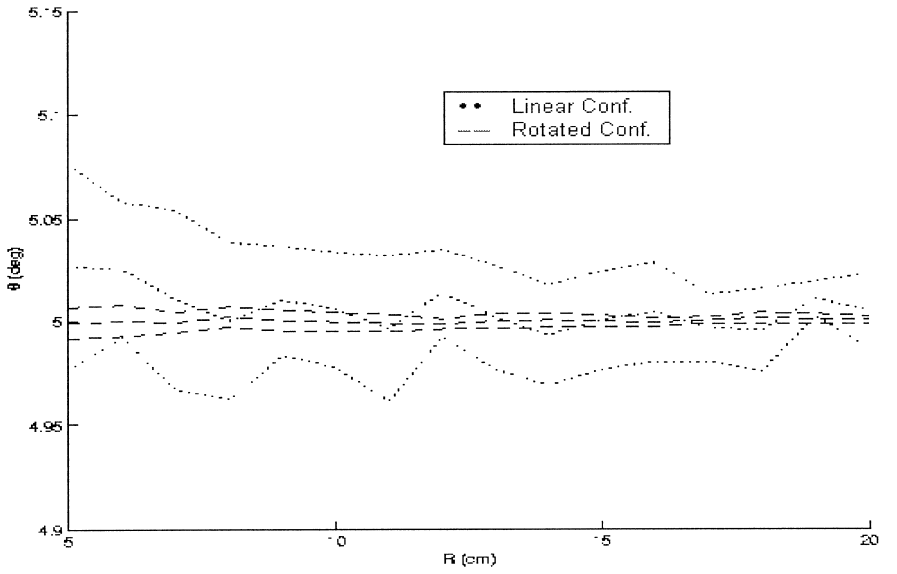

(b)

Fig. 6. Azimuth estimate (θ) versus (a) h_0, (b) R, with curve-fitting. Dotted and dashed lines indicate the mean of the estimate and $\pm\sigma_r$ obtained at the flat and adapted positions, respectively.

3.4. Comparison of TOF estimators

In this section, the bias, variance, and bias-variance combinations of the two TOF estimators are compared. In [28], in order to evaluate the performances of the estimators, the results are compared to the Cramér-Rao lower bound (CRLB) which sets a lower bound on the variance of unbiased estimators. The matched filter, which is the optimal method to estimate the time-of-flight, satisfies this lower bound asymptotically [29].

Fig. 7 illustrates variance σ^2, bias b_R, and $\sqrt{\sigma^2 + b_R^2}$, which is the combination of bias and variance terms, for R estimate with respect to the transducer separation d. Fig. 7(a) shows the results when the TOF is measured with the thresholding method and Fig. 7(b) displays the same results for the curve-fitting method. The difference between the bias-variance combinations is about 3-fold. The bias term for the thresholding method is about 10 times higher than that of the curve-fitting method, that is, the curve-fitting method decreases the bias on the estimates obtained by the thresholding method. Moreover, the variance term is dominant for the curve-fitting and the bias term is dominant for the thresholding.

4. Extended Kalman filtering

In this section, an extended Kalman filter (EKF) is used to estimate the location and radius of curvature of the target. The case in which the transducers are aligned is investigated. A detailed treatment of EKF can be found in [30].

4.1. Filter model

The following procedure is used to estimate the location and the radius of curvature of the cylindrical object.

- The state vector is defined as follows:

$$\mathbf{x}(k) \triangleq \begin{bmatrix} r(k) \\ \theta(k) \\ R(k) \end{bmatrix}$$

- The observation model is

$$\tilde{\mathbf{h}}(k) = \begin{bmatrix} h_0(k) \\ h_r(k) \\ h_l(k) \end{bmatrix} = \mathbf{h}[\mathbf{x}(k)] + \mathbf{w}(k)$$

where $\mathbf{w}(k)$ is zero-mean, additive, white Gaussian measurement noise and

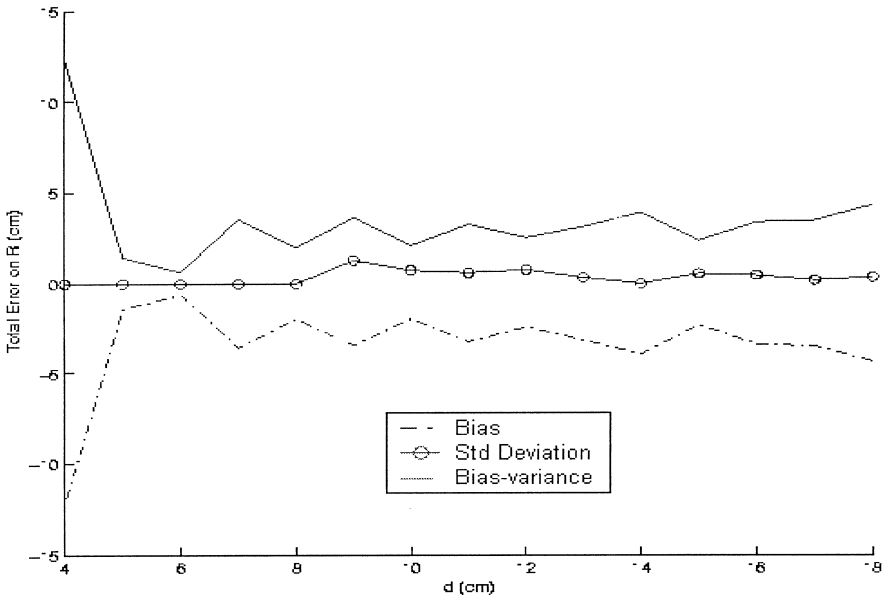

(a)

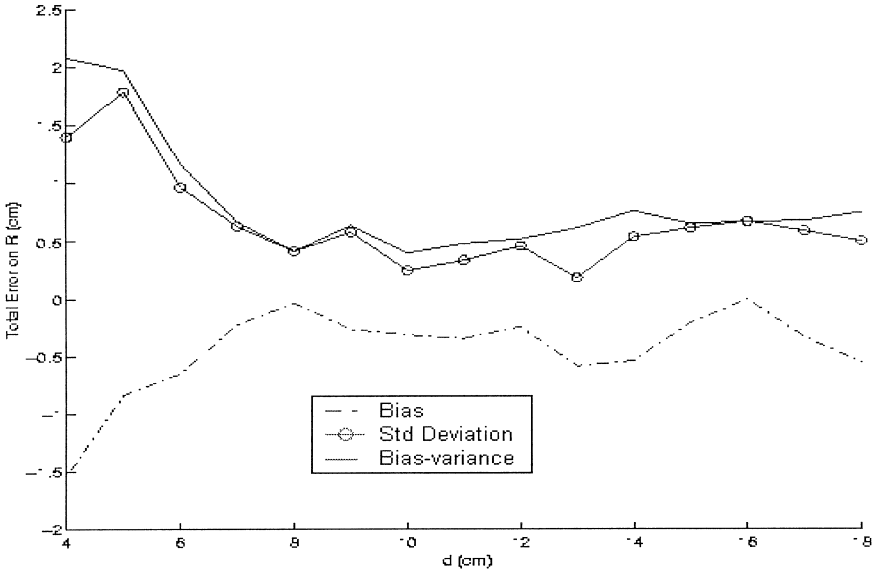

(b)

Fig. 7. *R* versus *d* with (a) thresholding, (b) curve-fitting. Standard deviation (dash-circle), bias (dash-dot), and bias-variance combination (solid) are shown.

$$\mathbf{h}[\mathbf{x}(k)] = \begin{bmatrix} r(k) - R(k) \\ \sqrt{r^2(k) + d^2 - 2dr(k)\sin\theta(k) - R(k)} \\ \sqrt{r^2(k) + d^2 + 2dr(k)\sin\theta(k) - R(k)} \end{bmatrix}$$

- Since the target is assumed to be stationary, the state-transition model is

$$\mathbf{x}(k+1) = \mathbf{F}\mathbf{x}(k) + \mathbf{v}(k) = \begin{bmatrix} r(k) \\ \theta(k) \\ R(k) \end{bmatrix} + \begin{bmatrix} v_r(k) \\ v_\theta(k) \\ v_R(k) \end{bmatrix}$$

where v_r, v_θ and v_R are the additive process noise for range, azimuth and radius, respectively. Note that, in this case, **F** matrix is an identity matrix. The state model in this case is linear, but the observation model is nonlinear.

- The Jacobian matrix **H** is found as follows:

$$\mathbf{H}(k) = \nabla\mathbf{h}(k) = \begin{bmatrix} -1 & 1 & 0 \\ -1 & \dfrac{r(k) - d\sin\theta(\mathrm{k})}{\sqrt{\mathrm{r(k)}^2 + d^2 - 2dr(k)\sin\theta(k)}} & - \dfrac{dr(k)\cos\theta(k)}{\sqrt{r(k)^2 + d^2 - 2dr(k)\sin\theta(k)}} \\ -1 & \dfrac{r(k) + d\sin\theta(k)}{\sqrt{r(k)^2 + d^2 + 2dr(k)\sin\theta(k)}} & \dfrac{\mathrm{d}r(k)\cos\theta(k)}{\sqrt{r(k)^2 + d^2 + 2dr(k)\sin\theta(k)}} \end{bmatrix}$$

where $r(k)$ and $\theta(k)$ are the predicted values of range and normal angle.

4.2. Simulation results

Fig. 8 illustrates the estimated states for the range, azimuth, and radius of curvature as the iteration number increases. For these figures, $d = 10$ cm, $R = 5$ cm, $h_0 = 100$ cm, $\theta = 0^\circ$, measurement noise standard deviation equals 10^{-6} V, the standard deviation of the radius noise equals 3.2×10^{-2} cm and standard deviation of the azimuth noise is 10^{-4} rad. As the iteration number increases, the estimated states converge to the actual values.

Fig. 9 displays the range, azimuth, and radius estimates by using raw data over a single data sequence (dash-dot lines) and extended Kalman filtering (solid lines). That is, in the first case, estimates are directly derived from the raw data, in the second, estimates are smoothed by the EKF. It is concluded that extended Kalman filtering smoothes the estimates considerably.

5. Experimental results

An experimental set-up using Polaroid transducers is employed to verify the simulation results by real sonar data from cylindrical targets.

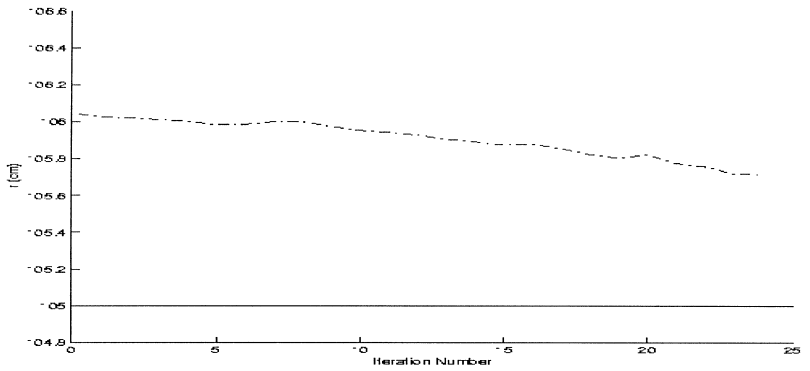

(a)

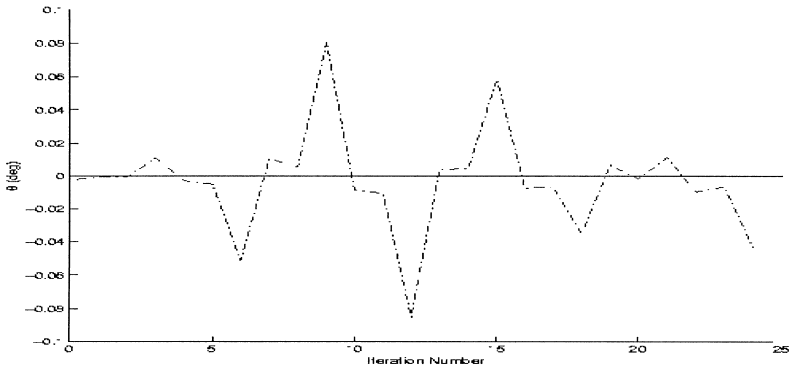

(b)

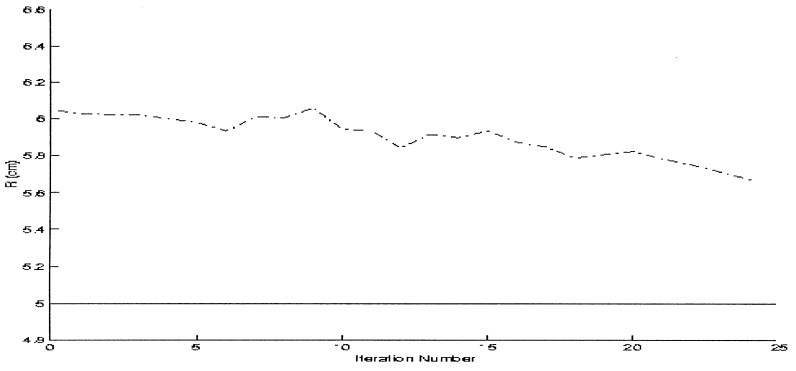

(c)

Fig. 8. Estimated states (a) r, (b) θ, (c) R.

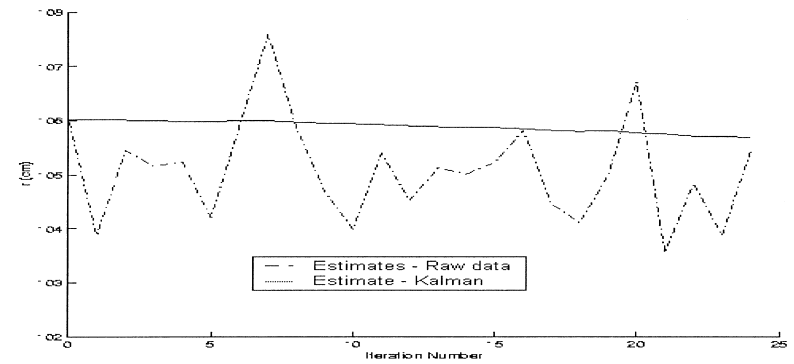

(a)

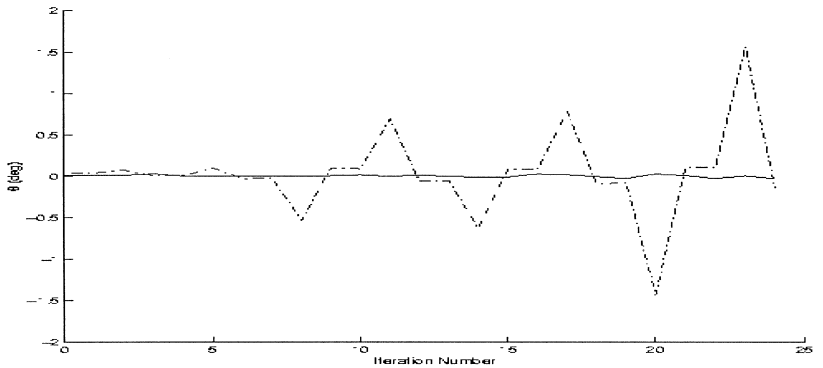

(b)

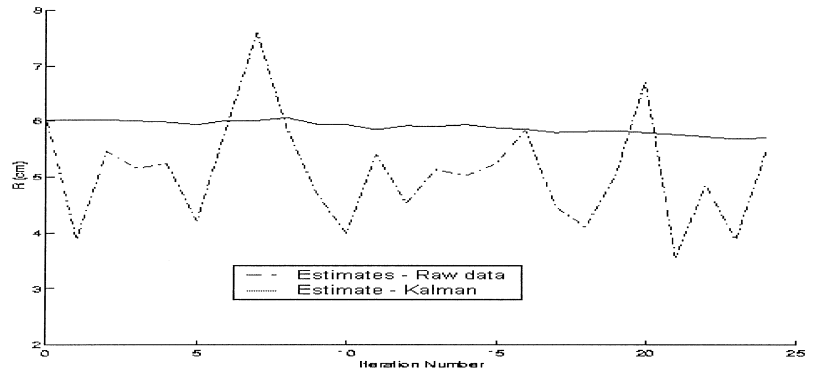

(c)

Fig. 9. Location and radius of curvature estimation versus (a) r, (b) θ, (c) R. Dash-dot and solid lines indicate the results obtained by using raw data over a single data sequence and Kalman filtering, respectively.

5.1. Experimental set-up

The set-up is constructed for 3-D applications. The unit illustrated in Fig. 10(a) comprises five Polaroid 6500 series acoustic transducers, each operating at a resonance frequency of $f_0 = 49.4$ kHz. A central transducer is flanked by four transducers symmetrically. The transducer separation d can be manually adjusted between 7.5 and 12.0 cm. The aperture radius, a, of each transducer is 2 cm. In the experiments, three of the transducers (left, right, and central) were used since the estimation was

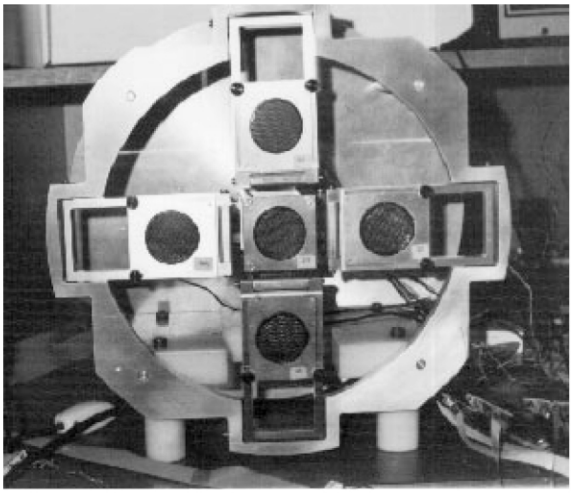

(a)

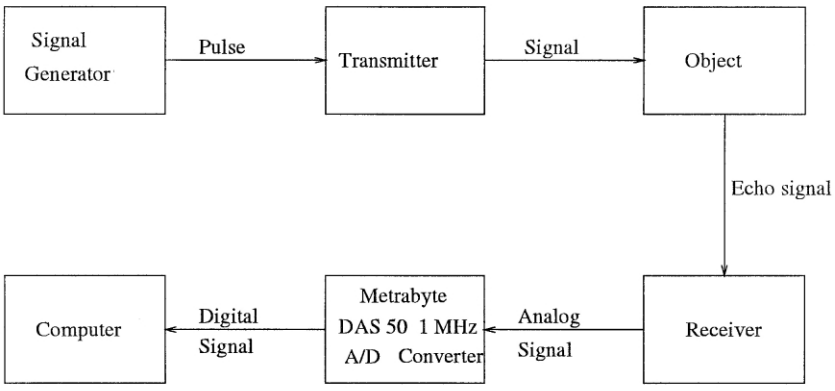

(b)

Fig. 10. The experimental set-up: (a) the sensing unit, (b) the block diagram of the sensing system.

done in 2-D for accurate calibration of the system. In some of the experiments, the transducers were detached from the mounting and were placed on polyamid stands so that larger transducer separations than allowed by the prototype system could be tested. The targets employed in this study are: cylinders with radii 25, 48, 75 mm and a planar target. All targets used in the experiments were wooden, with smooth surfaces, each with a height of 120 cm.

Ultrasonic transducers (acoustic transducers having a frequency higher than 20 kHz) are very suitable for target discrimination since they provide accurate range information. Although infrared-based systems have very high angular resolution, they do not provide very accurate range information [7]. As the resonance frequency of an ultrasonic transducer increases, the attenuation in air increases, the width of the main lobe decreases, and the number of the side lobes increases. In contrast, as the frequency decreases, the attenuation decreases, the number of side lobes decreases, but the width of the main lobe increases. The width of the main lobe is an indication of the angular resolution of the ultrasonic transducer. In this research, Polaroid transducers having a resonance frequency of 49.4 kHz are used although other ultrasonic transducers (e.g. Panasonic) having a resonance frequency around 40–60 kHz could also have been used. Polaroid transducers were chosen for the experiments since they are among the most widely available and commonly used transducers [31].

A four-channel DAS-50 A/D card with 12-bit resolution and 1 MHz sampling frequency is used to sample the analog signals reflected by the target. Echo signals were processed on an IBM-PC 486 using the C programming language. The block diagram for the hardware is shown in Fig. 10(b). Real distances were ascertained accurately by carrying out the whole set of experiments on large sheets of millimetric paper.

5.2. Results

For the same target position, 1000 sets of measurements, each having 10,000 samples of echo signals starting at the transmit time, were taken. Each set of measurements provides a single estimate of target radius of curvature, range and azimuth. It takes less than 0.5 s to gather a set of measurements and estimate the curvature, range, and azimuth. The pulse rate was set to around 17 pulses per s so that the maximum distance that could be measured is around 10 m. The pulse shape can be modeled as a sinusoidal enveloped by a Gaussian as described previously in Eq. (4).

In some of the experiments, the target was outside the joint sensitivity region for the chosen parameters. Therefore, in these experiments, the transducers' line-of-sights were maintained approximately perpendicular to the target surface during the process of data acquisition. The expected values [$E(r)$, $E(\theta)$, and $E(R)$] and standard deviations (a_r, a_θ, and a_R) of r, θ, and R estimates of each type of target considered are computed and tabulated in Tables 1–5. Table 6 illustrates the radius of curvature estimates for the flat and adapted positions of the transducers. The results before and after adaptation are denoted by the subscripts 1 and 2, respectively.

Table 1
Experimental results with thresholding when $\theta = 0^\circ$, $R = 75$ mm, and (a) $h_0 = 500$ mm θ (b) $h_0 = 600$ mm

d (mm)	$E(r)$ (mm)	θ_r (mm)	$E(\theta)$ (°)	σ_θ (°)	$E(R)$ (mm)	σ_R (mm)
(a)						
250	571.90	16.96	0.23	0.19	76.76	15.88
300	569.74	10.88	0.07	0.13	74.18	9.81
350	569.78	7.38	−0.06	0.15	73.66	6.82
400	569.73	5.27	0.11	0.19	73.89	8.09
450	570.07	4.93	−0.19	0.19	74.74	7.23
(b)						
250	661.73	15.93	0.36	0.16	73.26	15.17
300	663.84	15.15	0.21	0.10	74.87	13.90
350	661.98	13.02	−0.14	0.17	73.15	13.08
400	664.07	12.77	0.10	0.15	74.32	11.21
450	664.86	11.42	−0.43	0.15	74.45	9.91

Table 2
Experimental results with curve-fitting when $\theta = 0^\circ$, $R = 75$ mm, and (a) $h_0 = 500$ mm, (b) $h_0 = 600$ mm 40

d (mm)	$E(r)$ (mm)	θ_r (mm)	$E(\theta)$ (°)	σ_θ (°)	$E(R)$ (mm)	σ_R (mm)
(a)						
250	569.47	15.64	0.24	0.18	74.71	14.60
300	571.40	12.94	0.05	0.15	76.71	11.64
350	570.58	8.04	−0.09	0.15	74.59	7.25
400	569.45	8.75	0.12	0.18	73.57	8.02
450	569.51	8.36	−0.21	0.18	74.30	7.17
(b)						
250	664.49	17.71	0.13	0.24	75.80	20.85
300	664.04	16.43	0.05	0.13	75.14	15.23
350	667.68	17.49	−0.16	0.15	77.44	15.78
400	665.78	14.47	0.08	0.19	75.70	12.87
450	666.00	12.06	−0.40	0.20	75.40	10.53

Table 1(a) and (b) show, the estimates when the thresholding method is used for $h_0 = 500$ mm and $h_0 = 600$ mm, respectively. The true radius is $R = 75$ mm and the true azimuth angle is $\theta = 0^\circ$ for the two cases. As the transducer separation d increases, the standard deviations of the estimated range and radius decrease, but there is no observable trend in the standard deviation of θ. The error for $h_0 = 500$ mm is about 1.3% in the estimated radius and 0.9% in the estimated range. The error for $h_0 = 600$ mm is also about 1.3% in the radius estimation but 1.8% in the range estimation. Also, the standard deviations are in general larger for $h_0 = 600$ mm than for $h_0 = 500$ mm. Table 2 (a) and (b) illustrates the same results when the

Table 3
Experimental results when $h_0 = 600$ mm, $\theta = 0°$, and $R = 48$ mm with (a) thresholding, (b) curve-fitting

d (mm)	$E(r)$ (mm)	θ_r (mm)	$E(\theta)$ (°)	σ_θ (°)	$E(R)$ (mm)	σ_R (mm)
(a)						
250	637.96	24.18	−0.56	0.33	41.79	23.01
300	645.36	16.90	−0.11	0.12	49.16	15.38
350	643.29	13.03	−0.25	0.16	47.22	11.72
400	648.86	14.04	−0.18	0.19	52.30	12.68
450	643.10	10.26	−0.20	0.22	46.99	9.34
(b)						
250	645.27	29.32	−0.52	0.31	49.20	20.85
300	644.99	17.84	−0.12	0.13	48.92	15.23
350	648.39	14.86	−0.27	0.16	51.74	15.78
400	649.20	12.85	−0.16	0.24	52.76	12.87
450	643.41	12.84	−0.24	0.22	47.16	10.53

Table 4
Experimental results when $h_0 = 500$ mm, $d = 400$ mm, and $R = 25$ mm with (a) thresholding, (b) curve-fitting

θ(°)	$E(r)$ (mm)	θ_r (mm)	$E(\theta)$ (°)	σ_θ (°)	$E(R)$ (mm)	σ_R (mm)
(a)						
0	522.92	7.03	0.35	0.23	24.85	6.89
3	522.96	3.19	2.53	0.10	24.65	3.35
5	522.66	4.79	4.11	0.19	24.43	4.76
8	524.12	6.02	6.76	0.18	22.98	5.89
0	522.92	7.03	0.35	0.23	24.85	6.89
(b)						
0	522.81	6.76	0.39	0.26	24.76	6.66
3	522.73	4.45	2.52	0.14	24.50	4.10
5	524.19	5.54	4.20	0.21	26.01	5.30
8	525.91	6.41	6.81	0.20	24.71	6.19

curve-fitting method is used. The average error for the range is about 0.9% and it is 1.0% for the radius when $h_0 = 500$ mm and they are 1.3 and 2.2%, respectively, when $h_0 = 600$ mm.

Table 3 (a) and (b) displays the results for the thresholding and curve-fitting respectively when $h_0 = 600$ mm, true radius $R = 48$ mm, and true azimuth $\theta = 0°$. The standard deviations of the range and radius decrease as the separation d increases. The range estimation error is 0.8% for thresholding amid it is 0.7% for curve-fitting.

Table 4(a) and (b) illustrates the effect of the azimuth angle. As the azimuth angle increases, the standard deviations of the estimates tend to increase. Also, the estimates degrade as the true azimuth angle θ increases. The average error in the angle estimation is about 16% for thresholding and it is 11.4% for curve-fitting.

Table 5
Experimental results when $h_0 = 600$ mm, $0 = 0^\circ$ for a planar wall with (a) thresholding (b) curve-fitting

d (mm)	$E(r)$ (mm)	θ_r (mm)	$E(\theta)$ (°)	σ_θ (°)	$E(R)$ (mm)	σ_R (mm)
(a)						
200	3122.65	860.69	−0.01	4.12	2545.12	648.52
250	2561.10	693.35	−0.98	1.78	1981.51	688.54
300	1354.48	480.81	−1.20	3.14	775.72	476.15
(b)						
200	3503.52	830.69	−0.31	0.79	2924.89	929.26
250	2644.16	685.01	−0.54	1.76	2065.07	678.08
300	1467.02	103.38	−1.22	0.21	886.53	101.96

Table 6
Estimated radius at the flat and rotated positions with curve-fitting with respect to (a) d when $h_0 = 1000$ mm, $\theta = 0^\circ$, and $R = 75$ mm (b) 0 when $h_0 = 1000$ mm, $d = 75$ mm, $R = 25$ mm

	$E(R_1)$ (mm)	σ_{R_1} (mm)	$E(R_2)$ (mm)	σR_2 (mm)
d (mm)				
(a)				
150	73.61	20.49	76.29	12.50
200	72.65	18.87	73.46	10.96
250	...	–.	77.61	9.75
300	–	–.	72.28	8.31
350	–	–.	75.73	6.24
400	–	–	74.05	5.49
θ°				
(b)				
0	22.65	56.81	24.64	30.60
3	24.57	58.50	26.77	31.92
5	25.64	61.16	23.43	29.75

Table 5(a) and (b) tabulates the estimated results when the target is a plane. The radius of curvature estimations and the standard deviations are large. By looking at the radius of curvature estimates, it can be concluded that the object is a plane and the curve-fitting method gives better results.

Finally, Table 6(a) and (b) shows the radius of curvature estimates at the flat and rotated positions with respect to d and θ, respectively. Table 6(a) illustrates that the target at $h_0 = 1000$ mm remains outside of the joint sensitivity region at the fiat position when $d > 21$ cm. Therefore, for these cases, the transducers are maintained approximately perpendicular to the object surface while experimental data are being collected. It is observed that the standard deviation is less for the rotated position and estimates are closer to the true value. Table 6(b) tabulates the estimates for varying θ. The standard deviations at the flat position are almost twice those at the rotated positions. For larger values of θ than considered in Table 6(b), it is not possible to estimate the curvature since the target will be outside the sensitivity region of either the right or the left transducer.

6. Conclusion

In this study, an adaptive sensor configuration comprising three transmitting/receiving transducers has been introduced to estimate the position and radius of curvature of cylindrical objects. It has been shown that the estimates can be improved by approximately 40% with this sensor configuration when compared to the non-adaptive configuration. The simulation results and the comparison of the bias-variance terms indicate that the TOF measurements are improved by the curve-fitting method. Moreover, it has been shown that the extended Kalman filtering smoothes the estimates considerably.

The radius of curvature estimation provides valuable information for differentiating different types of reflectors such as edges, cylinders and walls. For large values of the R estimate, the target can be classified as a plane and for values close to zero, it can be classified as an edge. Current and future work will focus on improving the robustness of the radius of curvature estimation by using recursive digital filtering techniques. This will reduce the variance of the estimates and thus improve their reliability. More efficient firing techniques involving cross firing patterns will be considered to reduce the data acquisition time. In addition to TOF information, incorporation of amplitude information or the shape of the complete echo waveform in the current system will provide additional information about the location and curvature of the sonified target.

Since this paper was submitted, an alternative approach based on morphological processing, that can handle surfaces with spatially varying curvature which may become both concave and convex, has also been developed [32,33].

Acknowledgements

This work was supported by TÜBİTAK under projects 197E051 and EEEAG92 and the British Council Academic Link Program. The authors would like to thank the anonymous reviewers for their useful comments and suggestions.

References

[1] Barshan B, Kuc R. Differentiating sonar reflections from corners and planes by employing an intelligent sensor. IEEE Transactions on Pattern Analysis and Machine Intelligence 1990;12(6):560–9.
[2] Kleeman L, Kuc R. Mobile robot sonar for target localization and classification. International Journal of Robotics Research 1995;14(4):295–318.
[3] Kleeman L, Akbarally H. A sonar sensor for accurate 3-D target localization and classification. In: Proceedings IEEE International Conference on Robotics and Automation, Nagoya, Japan, 21–27 May 1995. p. 3003–8.
[4] Kuc R Fusing binaural sonar information for object recognition. In: Proceedings of IEEE/SICE/RSJ International Conference on Mtiltisensor Fusion and Integration for Intelligent Systems, 1996. p. 727–35.
[5] Kuc R. Biologically motivated adaptive sonar system. The Journal of the Acoustical Society of America 1996;100:1849–54.
[6] Kuc R. Biomimetic sonar recognizes objects using binaural information. The Journal of the Acoustical Society of America 1997;102:689–96.

[7] Flynn AM. Combining sonar and infrared sensors for mobile robot navigation. The International Journal of Robotics Research 1988;7(6):5–14.
[8] Curran A, Kyriakopoulos KJ. Sensor-based self-localization for wheeled mobile robots. Journal of Robotic Systems 1995;12(3):163–76.
[9] Peremans H, Audenaert K, Van Campenhout JM. A high-resolution sensor based on tri-aural perception. IEEE Transactions on Robotics and Automation 1993;9(1):36–48.
[10] Sabatini AM. Statistical estimation algorithms for ultrasonic detection of surface features. In: Proceedings IEEE/RSJ International Conference on Intelligent Robots and Systems, Munich, Germany, 12–16 September 1994. p. 1845–52.
[11] Ohya A, Ohya T, Yuta S. Obstacle detectibility of ultrasonic ranging system and sonar map understanding. Robotics and Autonomous Systems 1996;18:251–7.
[12] Sabatini AM. Adaptive target tracking algorithms for airborne ultrasonic rangefinders. IEE Proceedings-Radar Sonar and Navigation 1995;142(2):81–7.
[13] Sabatini AM. A digital signal processing technique for compensating ultrasonic sensors. IEEE Transactions on Instrumentation and Measurement 1995;44(4):869–74.
[14] Gibson I, Webb P, Wykes C. Robot guidance using ultrasonic arrays. Journal of Robotic Systems 1994;11(8):681–92.
[15] Ko JH, Kim WJ, Chung MJ. A method of acoustic landmark extraction for mobile robot navigation. IEEE Transcations on Robotics and Automation 1996;12(3):478–85.
[16] Smith AC, Searle GCL. Emprical observation of a sonar adaptive array. IEE Proc F, Commun Radar Signal Process 1985;132:595–7.
[17] Skolnik M. Introduction to radar systems. New York: McGraw-Hill, 1981.
[18] Barshan B. Fast processing techniques for accurate ultrasonic range measurements. Measurement Science and Technology 2000;11:45–50.
[19] Barshan B, Sekmen A. Radius of curvature estimation and localization of targets using multiple sonar sensors. The Journal of the Acoustical Society of America 1999;105(4):2318–31.
[20] Zemanek J. Beam behaviour within the nearfield of a vibrating piston. The Journal of the Acoustical Society of America 1971;49(1):181–91.
[21] Pierce AD. Acoustics, an introduction to its physical principles and applications. New York: McGraw-Hill, 1981.
[22] Barshan, B. A sonar-based mobile robot for bat-like prey capture. PhD thesis, Yale University, New Haven, CT, December 1991.
[23] Camp LW. Underwater acoustics. New York: Wiley-Interscience, 1970. p.166 (Chapter 7)
[24] Bozma, ÖI. A physical model-based approach to analysis of environrnents using sonar. PhD thesis, Yale University, New Haven, CT, May 1992.
[25] Ayrulu B. Classifications of target primitives with sonar using two non-parametric data fusion methods. MS thesis, Bilkent University, Ankara, Turkey, July 1996.
[26] Ayrulu B, Barshan B. Identification of target primitives with multiple decision-making sonars using evidential reasoning. The International Journal of Robotics Research 1998;17(6):598–623.
[27] Barshan B, Kuc R. A bat-like sonar system for obstacle localization. IEEE Transactions on Systems, Man and Cybernetics 1992;22(4):636–46.
[28] Sekmen A. Radius of curvature and location estimation of cylindrical objects with sonar using a multi-sensor configuration. MS thesis, Bilkent University, Ankara, Turkey, July 1997.
[29] Van Trees HL. Detection, estimation, and modulation theory, part I. New York: John Wiley & Sons, 1968.
[30] Bar-Shalom Y, Li X-R. Estimation and tracking: principles, techniques, and software. Boston: Artech House, 1993.
[31] Polaroid Corporation. Ultrasonic components group. 119 Windsor St., Cambridge, MA 02139, 1990.
[32] Başkent D, Barshan B. Surface profile determination from multiple sonar data using morphological processing. J Robotics Research 1999;18(8):788–808.
[33] Barshan B, Başkent D. Comparison of two methods of surface profile extraction from multiple ultrasonic range measurements. Measurement Science and Technology 2000;11(6):833–44.